

<2015>. This manuscript version is made available under the CC-BY-NC-ND 4.0 license <https://creativecommons.org/licenses/by-nc-nd/4.0/> This is the postprint version of an article accepted for publication in <Journal> (Elsevier). The Version of Record is available online at <https://doi.org/10.1016/j.apcatb.2014.10.031>

Photo-catalytical and antibacterial activity of TiO₂ nanoparticles obtained by laser ablation in water

M. Zimbone^a, M.A. Buccheri^a, G. Cacciato^b, R.Sanz^a, G. Rappazzo^c, S. Boninelli^a, R. Reitano^b, L. Romano^b, V. Privitera^a, M.G. Grimaldi^{a,b}

^a CNR-IMM, UOS (Università) via S. Sofia 64, 95123 Catania, Italy

^b Department of Physic and Astronomy University of Catania, via S. Sofia 64, 95123 Catania, Italy

^c Department of Biological, Geological and Environmental Sciences, via Androne 81, 95124 University of Catania, Italy.

Corresponding author: M.A. Buccheri CNR-IMM UOS (Università), via S. Sofia 64, 95123 Catania, Italy e-mail: mariaantonietta.buccheri@cnr.imm.it

ABSTRACT

This work focuses on the study of photo-catalytic and antibacterial activity of TiO₂ nanoparticles synthesized by laser ablation in water. The nanoparticles have a log normal size distribution with a mean diameter of 34 nm and are composed by a mixture of small crystallites and disordered TiO₂; they show good stability and are extremely pure. High photo-catalytic (methylene blue dye discoloration under UV illumination) and antibacterial (tested on *Escherichia coli*) activities comparable to that of commercial nanoparticles under the same experimental conditions were observed. Optical and structural properties were correlated to the photo-catalytic and antibacterial activity, and compared to that of commercial TiO₂ nanoparticles. An explanation of the high photoactivity yield is proposed taking into account the nanoparticles structure resulting from the peculiar synthesis procedure.

Keywords: Laser ablation in liquid, photocatalytical activity, antibacterial activity, nanoparticles

1. INTRODUCTION

Titanium oxide has received in the past 15 years a great interest both in the scientific community and in the industry, due to its properties such as photo-catalytic activity, hydrophilicity, stability, harmless (in bulk), and good economical yield. Taking the advantage of these properties, it is used in a wide range of applications as the decomposition of pollutants in air, water treatments, self-cleaning cover glasses and killing harmful bacteria [1][2].

Antimicrobial activity of TiO₂ was observed in 1985 by Matsunaga and colleagues, who reported that microbial cells could be killed by the contact with a TiO₂-Pt catalyst under illumination with near UV light [3]. Since then, many studies have investigated the disinfection potential of photo-catalysis using TiO₂, both powder and film, as photo-catalysts [3-6]. According to literature data, highly reactive oxygen species (ROS) are thought to be the key species in the photo-catalytic disinfection process. In fact, the photo-generated holes and electrons trapped on the surface of the semiconductor react with adsorbed species to initiate the formation of highly reactive oxygen species (ROS), •OH, O₂•⁻ and HO₂•, capable of mineralizing pollutants. All three ROS exhibit bactericidal activity but some studies have emphasized that the hydroxyl radical would be the most important oxidant species responsible for the attack of the bacterial cell wall, leading to modifications of membrane permeability and cell death. [4-6]

One of the most important applications of TiO₂, is the exploitation for water and air purification through utilization of solar energy [7]. Today, one of the biggest problems of humanity is the inadequate access to clean water. For this reason, much effort is devoted to study new efficient, low cost methods of purifying water, saving energy, and minimizing the consumption of chemical compounds to reduce their impact on the environment. Several methods have been developed for the realization of nano-structured titanium oxide membranes or films for developing very efficient photo-catalytic filters for water purification [8]. These nano-materials may be composed of nanofibers, nanotubes or nanoparticles [9-14], employing a variety of techniques such as plasma spray [15], anodization [16] and hydrothermal growth [17].

Synthesis of titanium oxide nanoparticles directly in liquid takes advantages of the simplicity of handling with low risk, and of the compatibility with other fabrication techniques such as spraying [15], dip or spin coating [18-20]. It is also compatible with membranes of polymeric nanocomposites [21-23].

Pulsed Laser Ablation in Liquids (PLAL) is one of the most promising techniques for the synthesis of oxide nanoparticles in liquids or in polymer matrices. It is a versatile, economical and “green” methodology that avoids the use of chemical reagents and reaction products, solving the problem of purification of nano-materials [24]. Moreover, it was recently demonstrated by Barcikowsky et al. that PLAL is also suitable for industrial purposes thanks to the high ablation rate (21 mg/min) [25] and the limited poly-dispersion [26-28]. The results reported in the literature concerning Ti ablation in water are controversial since some authors claim that the ablation of a titanium target in water results in the formation of metallic titanium nanoparticles [29], while others have obtained TiO_x particles [30,32] or a mixture of amorphous and crystalline phases [33]. Presumably the details of PLAL process have a strong impact on the properties of nanoparticles. Moreover, different experimental setup of PLAL may also influence photocatalytic and antibacterial activities [34,35]. Holes and electrons, generated through UV illumination, have to be separated and trapped onto surface defects in order to allow the electrochemical reaction with pollutants and water to proceed. In the case of TiO₂, photocatalytic activity strongly depends on the quantity and properties of surface defects (Ti interstitials, O vacancies, H inclusion or disorder) which, in turn, depend on the experimental setup of PLAL. Thus, it is reasonable that differences in the PLAL process may stem in nanoparticles with variable photocatalytic properties.

A systematic study of the combined photo-catalytic and antibacterial properties of titanium oxides obtained in defined ablation condition is lacking in our knowledge.

In this work, we report structural and optical characterization of the titanium oxide nanoparticles synthesised by PLAL in water by dynamic light scattering (DLS), UV-Visible spectroscopy (UV), scanning electron microscope (SEM), X-ray diffraction (XRD). The photo-catalytic activity of nanoparticles was evaluated by the discolouration of methylene-blue (MB) dye method and compared with that of commercial TiO₂ nano-powder. The antibacterial activity was tested on *Escherichia coli*, a well-known Gram-negative bacterium considered to be an indicator of faecal contamination in drinking water. Bacterial survival and the MTT assay were performed in comparison with commercial powder.

2. MATERIAL AND METHODS

2.1 PREPARATION

The synthesis of laser ablated nanoparticles (LA-Nps) was performed by the PLAL method. A Nd:YAG (Giant G790-30) 1064 nm laser (10 ns pulse duration, 10 Hz repetition rate) was employed to irradiate a titanium metal plate (Goodfellow, purity 99.9%, as rolled). The laser was focused using a lens (focal length of 20 cm), on the bottom of a teflon vessel filled with 5 ml of deionised Milli-Q water (resistivity 18 MOhm cm). The sample was irradiated at a fluence Φ of 5 J/cm² and the spot size was approximately 3.5 mm in diameter. The mass of the ablated material was estimated by weighting the target before and after the ablation with a micro analytical balance (Sartorius M5) with a sensitivity of 100 μ g. The titanium concentration in solution was calculated assuming that ablated material has been totally converted in nanoparticle.

Commercial standard TiO₂ nanoparticles (C-Nps) by Sigma Aldrich were used as a reference for the decolouration experiments. Each solution is obtained by dissolving 8 mg of powder in 8 ml of Milli-Q water (final concentration of 1 mg/ml) and stirring for 30 minutes.

2.2 METHODS

The UV-vis spectra were collected using a Perkin-Elmer Lambda 40 spectrometer in the wavelength range 350–900 nm with an integrating sphere (Labsphere 20).

DLS measurements were performed by a homemade apparatus as described elsewhere [36]: briefly the illumination source was a 660 nm diode laser whose power ranged between 15 and 150 mW, and the light scattered at 90° with respect the forward direction was recorded. The intensity auto-correlation function is obtained by a BI-9100 (Brookhaven Instruments Corporation) correlator working in photon counting regime. The field autocorrelation function, g_1 , is computed from the intensity autocorrelation function, g_2 , using the Segret relation ($g_2 = |g_1|^2$) [37] and is analyzed with second cumulant analysis method.

The samples for SEM, TEM and XRD measurements were produced drying a solution drop on substrates of copper foil, copper grid (covered with a holey carbon film) and glass respectively. Although some spurious effects can arise during and after the drying (particle–particle and particle–surface interactions), nonetheless the phase, shape, dimension and structure of the single nanoparticles are expected to be not influenced by these effects.

SEM images were acquired by using a Field Emission SEM (Gemini Zeiss SUPRA™ 25) at working distance of 5–6 mm, using an electron beam of 5 keV and an in-lens detector. ImageJ software was used to estimate the size of the nanoparticles.

TEM images were acquired by using a JEOL 2010 microscope operating at an acceleration voltage of 200 kV.

Crystal structure of the reference and synthesized nanoparticles was determined by X-ray diffraction (XRD, Bruker D-9000, Cu K α , 40 kV, 40 mA, at 0.01° s⁻¹) and Bruker diffraction suite software for the diffraction analysis. The Scherrer equation was applied to estimate the crystallite size.

In order to evaluate the photocatalytic activity of laser ablated nanoparticles dispersed in water, UV-photo-degradation test with Methylene-Blue (MB) dye was carried out. For these tests 20 μ L of MB solutions (0.05 wt. %) was added to the titanium oxide dispersion. Appropriate volumes of water were added up to 2 ml. The same preparation method was performed for commercial nanoparticles. The MB concentrations were measured applying the Lambert–Beer law at 664 nm (extinction coefficient 7.4 $\times 10^4$ M⁻¹cm⁻¹) after subtraction of background due to scattering. Moreover the scattering intensity gave us an independent indication of nanoparticle concentration. The solutions were left for one hour in dark to allow the absorption of MB onto nanoparticles and then, were illuminated by UV light. During the UV light irradiation the solutions were placed in a circular vessel of 2 cm² and covered with a quartz glass to avoid evaporation during irradiation. The wavelength of the UV light source was centred at 368 nm (FWHM lower than 10 nm) and UV irradiance was 1.1 mW/cm². The degradation rate was measured after 30 minutes of irradiation to overcome the non-linearity effects due to MB degradation kinetics [40].

Antibacterial activity of both C-Nps and LA-Nps was tested on *Escherichia coli* ATCC25922. A single colony was inoculated in 50ml of Luria-Bertani (LB) broth and grown overnight at 37°C by constant agitation at 180rpm under aerobic conditions. The following day, the bacterial growth was measured by optical density at 600nm.

CFU count. Bacteria were diluted up to 10⁸ CFU/ml and exposed either to C-Nps or LA-Nps at different concentrations in a volume of 2ml. ~~The bactericidal activity is due to the photocatalysis of TiO₂.~~

In order to test antibacterial activity, photo-catalysis was induced by exposition to the same UV light as for the MB photo-degradation. Untreated and exposed to UV only bacteria were treated in parallel as controls. Experiments were made in triplicates. Final concentrations of C-Nps and LA-Nps were tested, ranging from 25 to 100 µg/ml. Aliquots were collected at 15, 30 and 60 minutes respectively, conveniently diluted by serial dilutions 1:10 and plated in LB Agar Petri dishes. Plates were incubated overnight at 37°C. CFU were counted the following day.

MTT Assay. Bacteria were diluted up to 10^8 CFU/ml and exposed either to C-Nps or LA-Nps at different concentrations in a volume of 200µl. Final concentrations of C-Nps and LA-Nps were tested, ranging from 25 to 100 µg/ml. Untreated and exposed to UV only samples were run in parallel as controls. After 60 min exposition under the UV light, 100 µl were collected from each sample. MTT (10 µl) was added to each collected sample. Samples were incubated at 37°C for 2h in a thermostatic bath. After incubation, they were centrifuged at 8000 rpm for 3' and the supernatant discarded. Precipitated formazan crystals were resuspended in 200µl SDS10%, HCl 0,01N. After addition of 800µl of NaCl 0.9%, samples absorbance was measured at 575nm.

3.RESULTS

DLS and UV–Vis absorption spectra were carried out in order to characterize the colloidal solutions in liquid environment immediately after the ablation process.

Fig. 1a shows the UV–Vis spectra of laser ablated and commercial TiO₂ nanoparticles in distilled water. A strong absorption occurs below 400 nm in both samples; at longer wavelength the extinction of LA-Nps is definitely lower than that of C-Nps because of the scattering. In order to extract the absorption coefficient α from the extinction spectra, the contributions of the scattered light, fitted with an exponential law, has been subtracted.

It is well known that in direct bandgap or amorphous semiconductors the quantity $(\alpha h\nu)^r$ depends linearly on $h\nu$ being $r=2$ or $r=1/2$ respectively. In indirect bandgap semiconductors $\alpha^{1/2}$ is linear with $h\nu$ [39] and the band gap value is the intercept of the fit of the experimental curve with $h\nu$ axis.

In fig 1b the $\alpha^{1/2}$ versus $h\nu$ is reported for both LA-Nps and C-Nps. From the linear fit of the two curves result a band-gap of 3.13 eV and 3.18 eV for laser ablated and commercial nanoparticles, respectively, in agreement with generally accepted values [40]. In addition to that, in the insert of fig 1b a linear behaviour of $(\alpha h\nu)^{1/2}$ versus $h\nu$ in LA-Nps is evident at photons energy lower than 3 eV suggesting either the presence of a large amount of states inside the band-gap or a fraction of amorphous LA-Nps with a gap of 2 eV.

The hydrodynamic diameter and the mass of LA-Nps as a function of irradiation time are shown in fig 2a and b, respectively. At the initial stage, $t < 10$ min, large nanoparticles are formed at a rate of 30 $\mu\text{g}/\text{min}$, at longer times both nanoparticle diameter and the ablation rate saturate at 180 nm and 70 $\mu\text{g}/\text{min}$, respectively. In the inset of fig 2a the comparison between the intensity autocorrelation function of LA-Nps and C-Nps is shown. Cumulant analysis gives a decay time of 1.4×10^{-3} s and 8.5×10^{-3} s corresponding to a hydrodynamic diameter of about 181 nm and 1.1 μm for LA-Nps and C-Nps respectively.

It must be considered, however, that though DLS is a fast, non-destructive technique that allows measurement of nanoparticles size directly in solution, it overestimates the particle size in poly-disperse systems since the scattered light depends on diameter to the power of 6. To get the real LA-Nps size we performed SEM and TEM analysis on solid samples obtained by the drying of the solution. Figures 3a and 3c show a high resolution SEM and TEM image respectively of LA-Nps. The nanoparticles present spherical shape with well defined contour. The diameter histogram, obtained by the analysis of SEM image, is shown in fig 3b, and can be fitted with a log-normal distribution

$$P(d) = \frac{1}{\sqrt{2\pi}\sigma d} e^{-\frac{(\ln(d) - \ln(d_m))^2}{2\sigma^2}}$$

with a d_m of 34 ± 1 nm and σ of 0.5.

In the case of C-Nps compact aggregates of some microns in diameter are observed and showed fig 3d. These aggregates are constituted by smaller nanoparticles with mean size of 50 nm.

The nanoparticles stoichiometry was checked by RBS using a 2MeV He⁺ beam with a scattering angle of 165° in normal incidence. The RBS spectrum (showed in fig 1 of supporting information) shows signals from Ti, O, and Si. From the ratio of the Ti peak area to that of oxygen, the ratio [O]/[Ti] = 2.0 ± 0.1 has been evaluated. This stoichiometry is an averaged value since the film is composed by a random distribution of aggregated nanoparticles and it is not possible to evaluate the eventual oxidation profile over the particle structure.

XRD patterns obtained from LA-Nps and C-Nps are presented in fig 4. The diffraction pattern of the LA-Nps presents a very low intensity and broad peak (in the range 20°-30°) indicating the existence of a weak crystalline (disordered) structure. Despite of this broad spectrum the position of the peak is more compatible with anatase than rutile crystal phase though the presence of small amount of rutile cannot be excluded. Not taking into account lattice imperfections, possible inhomogeneous strains of the crystalline lattice, and assuming a unique anatase phase crystal, the average grain size of 2 nm can be estimated from the spectra by using the Debye-Scherrer approximation [41]. The presence of amorphous phase cannot be excluded on the basis of the XRD results. Indeed a broad peak compatible with an amorphous phase has been observed by Raman spectroscopy measurements (showed in fig 2 of supporting information). Another interesting point to be pointed out is the presence of hydroxyl groups, in dried LA-Nps, that has been evidenced in FTIR spectroscopy (showed in fig 3 of supporting information). H is identified by OH stretching at about 3400 cm^{-1} in FTIR spectra, as previously reported by Johnson et al. [42].

C-Nps have well defined crystal structure composed by anatase and rutile, with a mixture of approx 86% of anatase and 14 % of rutile, obtained by the relationship [43] $x = (1 + 0.8 \frac{I_{(101)}}{I_{(110)}})^{-1}$ where x is the

weight fraction of rutile in the powders, and $I_{(101)}$ and $I_{(110)}$ are the X-ray intensities of the anatase and rutile peaks, respectively in the position (101) (25.5°) and (110) (27.5 °).

From the merge of our analyses we can state that PLAL, in this particular experimental set-up, results in the formation of 34 nm sized hydrogenated TiO₂ nanoparticles. The phase of LA-Nps can be either a heavy defected very small anatase crystallites or a mixture of anatase and amorphous TiO₂ since the investigation so far performed do not allow discriminating between those.

The photocatalytic activity of LA-Nps was measured by means of the decolouration of methylene blue (MB) dye. In fig. 5a the absorption spectra of MB for different times of irradiation, in a solution of 50 µg/ml of LA-Nps, are shown. The spectra are normalized to that of the as-prepared solution. Using the absorption at 664 nm as a marker of MB concentration we plotted in fig 5b the MB concentration as a function of time for different LA-Nps concentrations in the range 5 µg/ml to 100 µg/ml exposed to UV. The graph includes the period preceding the UV exposition, given in negative values and denoted as dark in the graph, which reports the initial absorption of MB onto Nps.. The decrease of pure MB under illumination is also shown for comparison. No significant absorption of MB by Nps was detected as it is shown in the graph, thus the following reduction of MB concentration under UV exposure can be ascribed to the photocatalytic activity of Nps. The decrease of methylene-blue concentration under UV exposition follows a first-order kinetic law: $\ln C/C_0 = -k t$, where k is the decolouration rate. The results for several TiO₂ concentrations are summarized in fig 5c where the decolouration rate is reported as full dots. In the same graph, the decolouration rate of C-Nps is reported as open symbol. The data points from LA-Nps and C-Nps lie on a unique curve although the previously discussed difference between these particles.

Different concentrations of C-Nps and LA-Nps were tested for CFU counts and MTT assay, ranging from 25 µg/ml to 100 µg/ml. The best activity was obtained at the highest TiO₂ concentration (100 µg/ml). In fig 6a untreated and exposed to UV only bacteria, run as controls, are shown in the same figure. After 60' exposure to C-Nps, *E. coli* survival rate is around 25%. However, after 60' exposure to LA-Nps, bacterial survival rate was around 15%. Thus, LA-Nps display a slightly enhanced antibacterial activity if compared to the efficacy showed by the C-Nps.

MTT assay confirms results obtained by CFU count. After 60' exposure to C-Nps at the final concentration of 100 µg/ml, metabolism rate is reduced up to 22% whereas after 60' exposure to LA-Nps, metabolism rate is reduced up to 14%. This result is shown in the lower part (b) of fig 6. Again, LA-Nps show a slightly enhanced activity compared to C-Nps.

In both assays, the experimental error is around 5%. Differences in the antibacterial activity of LA-Nps and C-Nps, albeit small, are statistically significant, with $p < 0.01$, as assessed by a chi-square test performed on raw data.

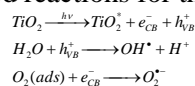
4. DISCUSSION

We first discuss the origin of LA-Nps size variation in water during irradiation. As seen in fig. 2, the hydrodynamic diameter reduces abruptly during the first ten minutes of irradiation (6×10^3 pulses) from 250 nm to the final steady state value of 180 nm caused by a variation of the nanoparticles morphology because of the re-irradiation of the nanoparticles dispersed in water. It has been shown that the absorption of the laser energy and the consequent melting or vaporization of the nanoparticles cause the reshaping or resizing, respectively [44]. In order to determine whether reshaping or size reduction may be caused by heating of particles, we estimated the temperature increase during the laser pulse. The adsorbed energy Q per particle is: $Q = \Phi \frac{\pi}{4} d^2 Q_{\text{abs}}$ where Φ is the photon fluence, Q_{abs} is the absorption Mie efficiency for spherical nanoparticles with diameter d . Q_{abs} was estimated by using the complex refractive index of bulk amorphous TiO_2 with a weak absorption due to non linear effects [45]. On the other hand absorption by defects is not expected to increase significantly Q_{abs} close to 1064 nm. The heat loss either by convective and radiative processes within 10 ns is considered to be negligible compared to the absorbed laser energy [44]. This clearly overestimates the real temperature reached by nanoparticles during irradiation. For a 5 J/cm^2 pulse and particles size of 34 nm (fig. 3), Q_{abs} was estimated to be lower than 10^{-3} ; the corresponding increase of temperature (calculated by $\Delta T = \frac{Q}{C_p \cdot m}$ where $C_p = 690 \text{ J}/\text{Kg}/\text{K}$ and m is the mass of the particle)

is estimated to be less than 900°C . The temperature rises is definitely lower than it is required to melt TiO_2 nanoparticle and a size variation, due to melting, seems very unlikely. We could invoke a variation of the target surface morphology and a consequent change in ablation conditions to justify the nanoparticle size variation. This would mean that there is an initial stage in which the target surface morphology varies. After that, when steady state is reached, the nanoparticles stabilize at constant value and the ablated mass is constant for each pulse (fig 2b).

A second point to be discussed is the possibility to generate amorphous or disordered nanoparticles by PLAL. In ambient conditions, the crystalline phases of TiO_2 are in general the most stable. In particular, anatase is preferred in particles smaller than about 11 nm, brookite between 11 and 35 nm, and rutile for larger particles [45-49]. The formation of the amorphous phase in LA-Nps could be ascribed to the fast, non-equilibrium quenching process and to the high temperature and pressure that are characteristic of the laser ablation process. During the laser ablation in liquids, high temperature and high pressure are generated on the target surface leading to the formation of a hot plasma plume over the laser spot [50]. High pressure (similar to those obtained during confinement of the plume inside the cavitation bubble) has been reported to cause the anatase-amorphous transition [51-53]. Moreover, being the plasma inside the cavitation bubble in water, it mixes with hydrogen, oxygen and water molecules, enhancing the temperature quenching [54-55] and realizing the Ti-O alloy. This process has been estimated to be 4 orders of magnitude more efficient than that required to quench the metastable amorphous phase [56-58].

We will discuss in the following the photocatalytic and antibacterial activity of TiO_2 . When titanium oxide absorbs the UV radiation, the generated electrons and holes have sufficient energy to catalyze the reaction of hydrolysis of water and to induce the formation of reactive oxygen species (ROS). These extremely active oxidizing species are responsible of the decomposition of several organic compounds [59-68] and of the antibacterial activity of TiO_2 [69]. The most important and generally accepted reactions for the ROS production are [70-75]:



Size, state of aggregation, exposed surface, amount of defects near the surface and also presence of the amorphous phase have a large effect on the activity of TiO_2 colloids.

Photocatalytic activity is measured by following the degradation of MB dye under UV irradiation. Indeed it is well known that MB can react with electron, holes or ROS species to give rise colourless products. As reported in figures 5a and 5b, discoloration of MB caused by the UV irradiation, in presence of LA-Nps, shows an exponential behaviour which resembles a first-order kinetic. The observed decolouration rate presents a linear trend with the concentration of LA-Nps in solution. LA-Nps show a similar steady state photo-catalytical efficiency of C-Nps, demonstrating a high photocatalytical activity, in despite of the low degree of crystallinity and the presence of amorphous phase.

LA-Nps antibacterial activity was tested by measuring the survival rate of *Escherichia coli* after exposure to UV light. *E. coli* is a well-known Gram-negative bacteria, it is a representative of coliforms and it is considered as an indicator of fecal contamination. International regulations on wastewater

treatment fix an upper limit of *E. coli* concentration in drinkable water. Hence, *Escherichia coli* has been chosen as a model organism. As shown in figure 6, LA-Nps are able to reduce bacterial survival to 15%, a result comparable to that obtained through C-Nps. Exposure of *Escherichia coli* to UV light in absence of TiO₂ reduced bacterial survival only up to 80%, thus damage due to UV light only is modest. Therefore, the majority of the effect is imputable to nanoparticles. In order to further investigate the antibacterial activity of LA-Nps, the MTT assay has been performed. MTT assay is based on the conversion of tetrazolium dye 3-(4,5-dimethylthiazol-2-yl)-2,5-diphenyltetrazolium bromide (MTT) into purple formazan crystals, by succinate dehydrogenase, a Krebs cycle's enzyme. Most respiring microorganisms are able to reduce tetrazolium dyes in their electron transport chain, generating results within hours [60]. Since in aerobic conditions, the respiratory activity is proportional to the number of viable cells, this assay is broadly used to measure in vitro cytotoxic effects. In our tests, MTT results confirm the observations made by CFU counts (Fig 6a). Our results show that in one hour LA-Nps are able to achieve an antibacterial activity slightly higher than C-Nps. The antimicrobial action of the TiO₂ photocatalyst has been ascribed to reactive oxygen species (ROS). Cho and colleagues demonstrated an excellent linear correlation between the amount of OH radical and the extent of *E. coli* inactivation in TiO₂ photocatalytic disinfection. They observed that the superoxide alone play a minor role in the inactivation mechanism of microorganisms while the OH radical is the primary species responsible for *E. coli* inactivation [69]. It is reasonable that a similar amount of ROS is generated by photo-catalysis for LA-Nps and C-Nps.

The high photocatalytic and antibacterial activity of LA-Nps may be ascribed to the presence of a disordered phase and to the high concentration of defects. In fact, the presence of defects like Ti interstitials, O vacancies, H inclusions can enhance the photo-activity of the crystalline TiO₂. In the most accepted mechanism of photo-catalysis, proposed by Fujishima [2], holes are trapped into surface defects and electrons localize into small hydrogen rich surface regions. This charges separation reduces the probability of recombination and increases the photo-catalytic effect. Following this idea, "black hydrogenated TiO₂" nano-crystals consisting of anatase core with a disordered H rich external shell, were recently synthesized [35]. The enhancement of the photo-catalytic activity was due to the "engineered disordered layer" caused by the incorporation of H onto the surface of the nanoparticles [36]. Moreover, it was recently demonstrated that Ti interstitials, and even more O vacancies, catalyze the O₂ adsorption and the scavenging of electrons with the consequent increase of the TiO₂ photo-activity [34]. In our case, nanoparticles have both a relatively high amount of defects or disordered layer, and H as detected by FTIR, due to the synthesis mechanism, and the surface stoichiometry can affect photo-activity properties. These features could make LA-Nps similar to black hydrogenated TiO₂ and this could be the reason of the high photo-catalytic and antibacterial activity. Moreover, aggregation has been reported as an improving factor of photocatalytic activity for the mixed phase anatase-rutile nanoparticles, since the migration of electrons across a phase junction was beneficial for charge separation [76]. Early studies suggested polymorphic characteristics to be one of the reasons for the high photocatalytic efficiency of C-Nps powder [77], this study is evidencing that even an amorphous component is relevant.

These two reported complementary arguments cannot be easily disentangled. Further analyses are necessary to improve the understanding of the mechanism for the high photo-catalytic activity for LA-Nps and in particular the role played by surface defects. The observed data can add relevant implications on the effects of TiO₂ polymorphisms on photocatalytic activity.

5.CONCLUSION

An extensive characterization of an alternative, industrially compatible and "green" synthesis of titanium oxides nanoparticles, with photo-catalytic activity and antibacterial properties comparable to commercial TiO₂ nanoparticles, is presented. The nanoparticles have a spherical shape, log normal size distribution with a mode of about 30 nm, and are well dispersed in liquid to ensure an effective large surface/volume ratio. They are shown to be a mixture of amorphous and very small (lower than 10 nm) nano-crystals. The decolouration rate of MB dye and antimicrobial activity, as assessed on *Escherichia coli*, were both comparable to those obtained with a highly active crystalline powder of commercially available TiO₂. Such high activity was correlated to the synthesis methodology and was attributed to the defects that prevent the electron-hole recombination. The efficient photo-catalytic rate, the antibacterial properties and the innovative synthesis make these nanoparticles an attractive option for a wide range of possible applications for water and air purification.

6. Acknowledgments

This work has been supported by the VII FP project Winning Applications of nanoTEchnologies for Resolutive hydropurification (WATER) funded by the European Commission (Grant 316082). The authors wish to thank Dr N. Piluso and F. La Via for Raman measurements.

Bibliography

1. K. Hashimoto, H. Irie, A. Fujishima, *J. Appl. Phys.* Vol. 44, No. 12, (2005), 8269
2. A. Fujishima, X. Zhang, D. A. Tryk, *Surface Science Reports* 63 (2008) 515
3. T. Matsunaga, T. Tomoda, T. Nakajima, H. Wake, *FEMS Microbiol. Lett.*, 29, (1985) 211.
4. G. Rincón, C. Pulgarin, *Appl. Catal. B: Environ.*, 44 (2003), pp. 263–284
5. A.K. Benabbou, Z. Derriche, C. Felix, P. Lejeune, C. Guillard, *Applied Catalyst B: Environmental* 76 (2007) 257–263.
6. S. Pigeot-Remy, F. Simonet, E. Errazuriz-Cerda, J.C. Lazzaroni, D. Atlan, C. Guillard. *Applied Catalysis B: Environmental*, 104 (2011), pp. 390–398
7. M. Pelaez, N. T. Nolan, S. C. Pillai, M. K. Seery, P. Falaras, G. Kontos, P.S.M. Dunlop, J.W.J. Hamilton, J.A. Byrne, K. O’Shea, M.H. Entezari, D.D. Dionysiou, *Applied Catalysis B: Environmental* 125 (2012) 331–349
8. G.E. Romanos, C.P. Athanasekou, V. Likodimos, P. Aloupogiannis, P. Falaras, *Ind. Eng. Chem. Res.*, 2013, 52 (39), pp 13938–13947
9. L. Liu, Z. Liu, H. Bai, D.D. Sun, *Water Res.* 2012, 46, 1101–113
10. H. Bai, Z. Liu, D.D. Sun, *Appl. Catal.-B Environ.* 2012, 111–112, 571.
11. D. Fang, Z. Luo, K. Huang, D.C. Lagoudas, *Appl. Surf. Sci.* 2011, 257, 6451–21.
12. W. Choi, N.-S. Park, M.R. Wiesner, J.-O. Kim. *Water Sci. Technol.* 2010, 62, 963–22,
13. J. Liao, S. Lin, N. Pan, D. Li, S. Li, J. Li, *Chem. Eng. J.* 2012, 211–212, 343–23
14. G. Pilatos, E.C. Vermisoglou, G.E. Romanos, G.N. Karanikolos, N. Boukos, V. Likodimos, N.K. Kanellopoulos, *Adv. Funct. Mater.* 2010, 20, 2500–24,
15. Y.-F. Lin, K.-L. Tung, Y.-S. Tzeng, J.-H. Chen, K.-S. Chang, *J. Membrane Sci.* (2012), 389, 83.
16. A. Chaudhary, T. H. Choudhury, S. Naik, S. Raghavan, *J. Am. Ceram. Soc.* Volume 95, Issue 1, pages 64–66, January 2012
17. A. Hu, X. Zhang, K. D. Oakes, P. Peng, Y. N. Zhou, M. R. Servos, *J. Hazard. Mater.* 2011, 189, 278.
18. H.-J. Hong, S. K. Sarkar, B.-T. Lee, *J. Eur. Ceram. Soc.* 2012, 32, 657.
19. X.P. Cao, D. Li, W.H. Jing, W.H. Xing, Y.Q. Fan, *J. Mater. Chem.* 2012, 22, 15309.
20. X. Wang, F. Shi, W. Huang, C. Fan, *Thin Solid Films.* 2012, 520, 2488.
21. M. Lombardi, P. Palmero, M. Sangermano, Varesano, Volume 60, Issue 2, pages 234–239, February 2011
22. H. R. Pant, B. Pant, P. Pokharel, H.J. Kim, L.D. Tijing, C.H. Park, D.S. Lee, H.Y. Kim, C. S. Kim, *J. Membrane Sci.* 2013, 429, 225–18
23. X. Ding, S. Zhou, L. Jiang, H. Yang, *Sci. Tech.* 2011, 58, 345.
24. S. Besner, A.V. Kabashin, F.M. Winnik, M. Meunier, *Appl Phys A* (2008) 93: 955–959
25. C. L. Sajti, R. Sattari, B. N. Chichkov, S. Barcikowski, *Phys. Chem. C* 2010, 114, 2421–2427
26. D. Werner, T. Ueki, S. Hashimoto, *J. Phys. Chem. C* 2012, 116, 5482–5491
27. F. Mafune, J. Kohno, Y. Takeda, T. Kondow, *J. Phys. Chem. B*, Vol. 106, No. 31, 2002
28. A. Pyatenko, M. Yamaguchi, M. Suzuki. *J. Phys. Chem. C* 2009, 113, 9078–9085
29. N.G. Semaltianos, S. Logothetidis, N. Frangis, I. Tsiaoussis, W. Perrie, G. Dearden, K.G. Watkins, *Chemical Physics Letters* 496, (2010). 113.
30. A. De Bonisa, A. Galassoa, N. Ibris, A. Lauritaa, A. Santagata, R. Teghil, *Applied Surface Science.* 2013
31. C. Huang, J. Bow, Y. Zheng, S.Y. Chen, N.J. Ho, P. Shen, *Nanoscale Res Lett* (2010) 5:972–985
32. A.S. Nikolov, P.A. Atanasov, D.R. Milev, T.R. Stoyanov, A.D. Deleva, Z.Y. Peshev. *Applied Surface Science* 255 (2009) 5351–5354]
33. M. Boutinguizaa, J. del Vala, A. Riveiroa, b, F. Lusquiñosa, F. Quinteroa, R. Comesañac, J. Poua* *Physics Procedia* 41 (2013) 780–786
34. C. L. Muhich, Y. Zhou, A. M. Holder, A. W. Weimer, and C. B. Musgrave. *J. Phys. Chem. C*, 2012, 116 (18), pp 10138–10149
35. X. Chen, L. Liu, P. Y. Yu, S. S. Mao *Science* Vol. 331 No. 6018 (2011) 746–750
36. M. Zimbone P. Musumeci P. Baeri E. Messina S. Boninelli G. Compagnini L. Calcagno, *J. Nanopart. Res* (2012) 14:1308
37. B. Berne, R. Pecora *Dynamic Light Scattering*. Wiley, New York Berne And Pecora 1976

38. C. Yogi, K. Kojima, N. Wada, H. Tokumoto, T. Takai, T. Mizoguchi, H. Tamiaki *Thin Solid Films* 516 (2008) 5881–5884
39. M. Takagi, *J. Phys. Soc. Jpn.* 1954, 9, 359.
40. F. Barreca, N. Acacia, E. Barletta, D. Spadaro, G. Currò, F. Neri, *Applied Surface Science* 256 (2010) 6408–6412
41. B.D. Cullity, *Elements of X-Ray Diffraction*, Addison–Wesley, 1978.
42. O. W. Johnson, John DeFord and J. W. Shaner, *J. Appl. Phys.* 44 (1973) 3008.
43. R.A. Spurr, H. Myers, *Anal. Chem.* 29 (1957) 760.
44. C. C. Evans, J. D. B. Bradley, E. A. Martí-Panameño, E. Mazur *Optics Express*, Vol. 20, Issue 3, pp. 3118-3128 (2012)
45. H. Zhang, J. F. Banfield, *J. Phys. Chem. B* 2000, 104,
46. G. Guisbiers, O. Van Overschelde, M. Wautelet, *Applied Physics Letters* 92, (2008) 103121
47. H. Zhang, J. F. Banfield, *J. Mater. Chem.*, 1998, 8(9), 2073–2076
48. S. C. Singh, R. Gopal, *R Bull. Mater. Sci.* 30, (2007) P. 291.
49. M. Boutinguiza, J. del Val, A. Riveiro, F. Lusquiños, F. Quintero, R. Comesaña, J. Pou *Physics Procedia* 41 (2013) 780 – 786
50. A. De Giacomo, M. Dell’aglio, A. Santagata, C. R. Gaudio, O. De Pascale, P. Wagener, G. C. Messina, G. Compagnini, S. Barcikowski, *Phys Chem Chem Phys.* 2013 Mar 7, 15(9):3083-92
51. V. Swamy, A. Kuznetsov, L.S. Dubrovinsky, R.A. Caruso, D.G. Shchukin, B.C. Muddle, *Phys. Rev. B* 71, 184302 (2005)
52. G.W. Yang, *Prog. Mater. Sci.* 52, 648 (2007)
53. S.R. Elliott, *Physics Of Amorphous Materials*, 2nd Edn. (Longman Sci. Tech., Essex, 1990)
54. T. E. Itina, *J. Phys. Chem. C* 2011, 115, 5044–5048
55. N.G. Semaltianos, S. Logothetidis, N. Frangis, I. Tsiaoussis, W. Perrie, G. Dearden, K.G. Watkins *Chemical Physics Letters* 496 (2010) 113–116
56. C. Pan, P. Shen, S.Y. Chen, *J. Crystal Growth* 299, 393 (2007)
57. C.G. Levi, V. Jayaram, J.J. Valencia, R.J. Mehrabian, *J. Mater. Res.* 3, 969 (1988)
58. S.Y. Chen, P. Shen, *Phys. Rev. Lett.* 89, 096106 (2002)
59. Ma Y, Yao J (1999) *Chemosphere* 38:2407
60. M.V. Berridge, P.M. Herst, A.S. Tan, *Biotechnol Annu Rev.* 2005;11:127-52
61. M. Cho, H. Chung, W. Choi, J. Yoona *Water Research* 38 (2004) 1069–1077
62. R. Comparelli, E. Fanizza, M. L. Curri, P. D. Cozzoli, G. Mascolo, R. Passino, A. Agostiano 2005 *Appl. Catal. B* 55 81
63. H. Haick, Y Paz 2003 *J. Phys. Chem. B* 107 2319
64. M.-S. Wong *Et Al* 2006 *Appl. Environ. Microbiol.* 72 6111
65. Z. X. Lu, L. Zhou, Z. L. Zhang, W. L. Shi, Z. X. Xie, H. Y. Xie, D. W. Pang, P. Shen 2003 *Langmuir* 19 8765
66. G. Fu, P. S. Vary, C. T. Lin *J. Phys. Chem. B* (2005) 109 8889
67. L. K. Adams, D. Y. Lyon, P. J. Alvarez *J. Water Res.* (2006) 40 3527
68. G. Gogniat, M. Thyssen, M. Denis, C. Pulgarin, S. Dukan (2006) *Fems Microbiol. Lett.* 258 18
69. Cho M., Chung H., Choi W., Yoona J. *Water Research* 38 (2004) 1069–1077
70. B. Lee, W. Liaw, J. Lou *Environ Eng Sci* 16:165 (1999)
71. S. Lakshmi, R. Renganathan, S. Fujita (1999) *J Photochem Photobiol A Chem* 127:123
72. X. Li, G. Liu, J. Zhao, *New J Chem* 23 (1999) 1193
73. NR Tacconi, J Carmona, K Rajeswar (1997) *J Electrochem Soc* 144:2486
74. T. Tatsuma, S. Tachibana, T. Miwa, DA. Trky, A. Fujishima (1999) *J Phys Chem B* 103:8033
75. Y Ma, J Yao (1999) *Chemosphere* 38:2407
76. Y. K. Kho, A. Iwase, W. Y. Teoh, L. Mädler, A. Kudo, R. Amal, *J. Phys. Chem. C* 2010, 114, 2821-2829
77. W. Y. Teoh, J. A. Scott, Rose Amal, *J. Phys. Chem. Lett.* 2012, 3, 629-639

Figure caption

Figure 1: (a) UV–Vis spectra of laser abated titanium oxide nanoparticles and commercial TiO₂ nanoparticles in water. (a) $(\alpha)^{1/2}$ versus $h\nu$ plot for indirect band gap transition for laser ablated and commercial nanoparticles. A band-gap of 3.13 eV and 3.18 eV for laser ablated and commercial nanoparticles respectively can be extracted from the intercept of the fit of the experimental curve with $h\nu$ axis (b) Tauch plot for amorphous $(\alpha h\nu)^{1/2}$ versus $h\nu$ for LA-Nps together with the straight line fit.

Figure 2: Hydrodynamic diameter (a) and ablated mass (b) as a function of ablation time. In the insert, DLS autocorrelation functions for LA-Nps and C-Nps in semi-log scale.

Figure 3: (a) High resolution FE-SEM image of LA-Nps. (b) Size distribution of LA-Nps together with a log-normal distribution fit. (c) High resolution TEM images of LA-Nps. (d) SEM image of C-Nps.

Figure 4: XRD pattern of LA-Nps and C-Nps. Vertical lines indicate the position of the main anatase (dash line at 25.5° A(101)) and rutile (dash-dot line at 27.5° R(110)) peaks.

Figure 5 (a) Absorption spectra of MB after UV irradiation for different times in a 50 ug/ml solution of LA-Nps. (b) Relative MB absorption at 664 nm as a function of irradiation time. Concentration of LA-Nps ranges from 5 ug/ml to 100 ug/ml. (c) Decolouration rate of LA-Nps and C-Nps as a function of the amount of titanium. A linear fit of LA-Nps decolouration rate is also shown.

Figure 6: Antibacterial activity test. Relative *E.coli* survival rate for CFU count (a) and relative values of absorbance measured at 575nm for MTT assay (b) after 60' exposure to LA-Nps and C-Nps. Untreated control and UV control were run in parallel.

Figure 1 SI: RBS spectra of a dried LA-Nps. RBS was performed by using a 2MeV He⁺ beam with a scattering angle of 165° in normal incidence. The solid sample was prepared by drying a solution drop on a silicon substrate. This procedure leaves a thin layer of Nps over the Si face. Signals from Ti, O, and Si are evident. From the ratio of the Ti peak area to that of oxygen, the ratio $[O]/[Ti]= 2.0\pm 0.1$ has been evaluated.

Figure 2 SI: Raman spectra of LA-Nps, amorphous, anatase and rutile TiO₂ film. Raman spectra were collected by using a HR800 integrated system by Horiba Jobin Yvon in a back-scattering configuration with a grating with 2400gr/mm. The excitation wavelength is supplied by a He-Cd laser (325 nm) with a penetration depth is 16 nm.

Figure 3 SI: FTIR absorbance measurements of dried LA-Nps. Hydroxyl groups were identified by OH stretching at about 3400 cm^{-1} and TiO₂ features were identified at 750 cm^{-1} . Measurements were performed with a Perkin Elmer FTIR SPECTRUM 1000 in the wavenumber range between 500 and 4000 cm^{-1} with a resolution of 2 cm^{-1} .